Effects of Anatomical Variations of the Stomach on Body-Surface Gastric Mapping Investigated Using a Large Population-Based Multiscale Simulation Approach

Kanyarak Ruenruaysab, Stefan Calder ⓘ, Tommy Hayes, Christopher N. Andrews, Gregory O'Grady, Armen Gharibans, and Peng Du ⓘ

Abstract—Body-surface gastric mapping (BSGM) measures the resultant body-surface potentials of gastric slow waves using an array of cutaneous electrodes. However, there is no established protocol to guide the placement of the mapping array and to account for the effects of biodiversity on the interpretation of BSGM data. This study aims to quantify the effect of anatomical variation of the stomach on body surface potentials. To this end, 93 subject specific models of the stomach and torso were developed, based on data obtained from the Cancer Imaging Archive. For each subject a set of points were created to model general anatomy the stomach and the torso, using a finite element mesh. A bidomain model was used to simulate the gastric slow waves in the antegrade wave (AW) direction and formation of colliding waves (CW). A forward modeling approach was employed to simulate body-surface potentials from the equivaelent dipoles. Simulated data were sampled from a 5×5 array of electrodes from the body-surface and compared between AW and CW cases. Anatomical parameters such as the Euclidean distance from the xiphoid process (8.6 ± 2.2 cm), orientation relative to the axial plane ($195 \pm 20.0°$) were quantified. Electrophysiological simulations of AW and CW were both correlated to specific metrics derived from BSGM signals. In general, the maximum amplitude ($\Delta\phi$) and orientation (θ) of the signals provided consistent separation of AW and CW. The findings of this study will aid gastric BSGM electrode array design and placement protocol in clinical practices.

Index Terms—EGG, BSGM, gastric slow waves, FEM, BEM.

I. INTRODUCTION

MOTILITY (contraction) of the stomach is a critical aspect of digestion, as it serves to break down the ingested food and mix with gastric secretions. There are number of co-regulatory physiological systems that govern gastric motility, and chief among them is an electrophysiological activity called slow waves, which are generated and propagated by specialized pacemaker cells called the interstitial cells of Cajal (ICC) [1]. Recent clinical evidence has highlighted the role of gastric slow wave dysrhythmias in disorders that are related to the abnormal motility of the stomach, such as gastroparesis, functional dyspepsia, reflux and nausea & vomiting [2], which are prevalent and challenging to manage.

Normal gastric slow waves propagate in the antegrade direction along the stomach at a rate of approximately three cycles per minute (cpm) in humans [3]. Applications of multi-channel high-resolution (HR) electrical mapping from the serosal surface of the stomach during surgery have revealed that human gastric slow waves originate from a pacemaker region in the proximal stomach, along the greater curvature. Slow waves then propagate in a circumferential direction to form a ring around the gastric lumen and then propagate towards the pylorus with varying amplitude and velocity, i.e., slower in the corpus (2.6–3.5 mm·s^{-1}) and faster in the distal antrum (4.7–6.9 mm·s^{-1}) [4]. It takes approximately 60 s for a single cycle of slow waves to reach the pylorus, resulting in three or more simultaneous wavefronts propagating in the human stomach [5].

Although well defined, the nominal frequency range of gastric slow waves in unto itself is not a clinically diagnostic measure. As recent clinical HR mapping in motility disorders have revealed persistent spatial dysrhythmias that often occurred within the nominal frequency range [6]. One of the common spatiotemporal abnormalities observed was an abnormal conduction in the form of a colliding wavefront (CW) between the normal antegrade wavefront (AW) and a retrograde wavefront from an ectopic pacemaker originated in the distal stomach [6].

While offering high fidelity data, serosal HR mapping is limited by its invasive deployment. Additional studies have attempted to minimize the invasiveness by developing laparoscopic or endoscopic electrodes [7], [8]. In both cases recordings are still limited to a short duration (<20 min), and the anesthetic and sedation protocol required meant the stomach is not in its normal physiological state. To

circumvent this problem, electrogastrography (EGG), which involves placement of cutaneous electrodes directly above the stomach in the epigastrium region of the torso, is applied by researchers. Conventional EGG analysis is principally focused on frequency metrics [9], [10], but more recently a body-surface gastric mapping (BSGM) approach, involving multiple EGG electrodes (>20 electrodes), has shown promise to capture both frequency and spatial changes of gastric slow waves, as well as presenting a strong correlation with symptoms [11].

A major challenge for analysis of BSGM is to account for the variations in the size and orientation of the stomach in relation to the torso [12], [13]. The lack of an optimal electrode placement procedure makes it difficult to compare results across different studies and individuals. A previous simulation study has attempted to address this issue by changing the orientation of the stomach inside a single torso model using a forward simulation approach [14], but realistic anatomical variables were not captured. Moreover, investigations have shown the need for optimal placement to account for realistic anatomical variations, but it could not be determined due to limited sample size [14]. The coverage of the body-surface by the electrode array was also shown to be an important factor in capturing changes in slow wave propagation in a previous clinical study [15].

The main objective of this study was to conduct a large modelling-based population study of the effects of realistic variations of stomach and torso anatomies on BSGM potential distributions. This work refined the previously-described methodologies of model development [14], [16], and extended it to a large sample size (n = 93), as well as comparing the differences between normal and retrograde gastric slow waves. The results presented in this paper will inform coverage and potential target area of the torso for placement of electrodes to obtain signals that are sufficient in capture the difference between consistently antegrade and colliding gastric slow wave propagations.

II. METHODOLOGY

The workflow of this study is divided into three main components. The first component involved manual segmentation of the stomach and torso outlines, as well as marking the key anatomical landmark points on the torso. The second component involved developing a three-dimensional (3D) anatomical model of the stomach and torso of each individual based on the segmented data. Finally, the third component involved performing simulations of normal and a common dysrhythmic activity, colliding wavefronts in the distal stomach, using a combination of finite element method (FEM) and boundary element method (BEM) [17]. The simulated body-surface potentials were analyzed in relation to the anatomical variations and the different types of gastric slow waves.

A. Image Source and Segmentation

CT scans of 93 different human stomach and torsos were acquired from an open-access database of medical images, The Cancer Imaging Archive (TCIA) [18]. The main selection criteria were no known surgical or pathological changes to the
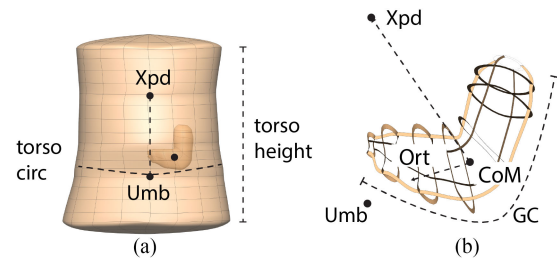

Fig. 1. Overview of the development of the stomach and torso models. (a) A subject specific torso and stomach model. The xiphoid (Xpd) and umbilicus (Umb) position were labeled manually based on the CT image. From the torso model, the circumference (torso circ) and torso height were calculated. (b) The distance between the xiphoid and center-of-mass (CoM) of the stomach, as well as the length of the greater curvature (GC) was calculated. The orientation of the stomach (Ort) was calculated as the average angles along the longitudinal axis, relative to the axial plane.

stomach. The group consisted of 60 male and 33 female patients with the average age of 67 ± 10 years.

Manual segmentation of the CT images was done by a medical trainee using ITK-SNAP [19], under senior clinical supervision. Cases where the cancer affected gastric anatomy were excluded. The cross-section of the stomach was labeled on a select number of slices, depending on how well the segmentations represented the whole shape of the stomach, usually in the coronal plane. After the cross-section mask was labeled, a different marker placed eight pairs of points along the lesser and greater curvature, respectively. The midpoint intersecting across each pair of points was assumed to be the center of the stomach that also followed the long gastric axis. Two additional pairs of points at each level were generated by rotating the manually marked pair of points by 90 degrees around the long gastric axis. The centroid of the stomach was calculated as the center-of-mass of the 16 points that defined the 3D outline of the stomach.

The xiphoid process and umbilicus were also manually labeled, along with the widest points of the torso on the left and right of the hip as well as the back, on the same axial plane as the umbilicus. The widest points of the torso were labeled on four other axial planes: 1) same plane as xiphoid, 2) 100 mm below umbilicus, 3) 100 mm above umbilicus, and 4) midway between the umbilicus and xiphoid. Some CT scans did not cover a field that was large enough to place labels 100 mm below (or above) the umbilicus (or xiphoid). Hence, the transverse placements of the proximal and/or distal torso outline were estimated from an axial projection of the most proximal and/or distal image slice. Altogether, the 20 data points were manually labeled for each torso.

B. Anatomical Models Development

Fig. 1 illustrates an example torso model with the subject-specific embedded stomach model. Models of the stomach and torso were developed from the manually labeled points using the finite element method. Specifically, cubic Hermite basis function (derivative continuous) was fitted in the circumferential direction of the stomach to form an ellipsoid and a linear basis function was used to join the ellipsoids together to form a surface
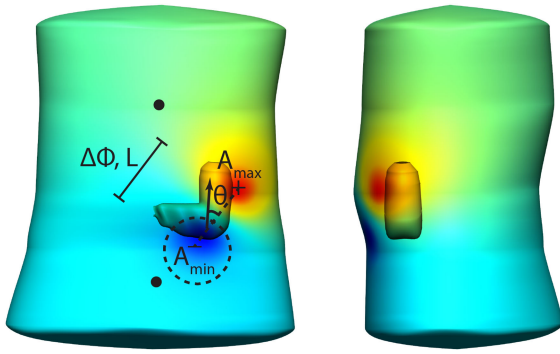
Fig. 2.   Overview of the development of the stomach and torso models. (a) The stomach segmentations on the coronal place were used to develop the geometry of the stomach. (b) The torso geometry was developed from skin landmarks on the axial slices.

mesh of the stomach. The surface mesh was then projected inwards in the transmural direction by 3 mm to represent the thickness of gastric wall [20], as shown in Fig. 1(b). A linear basis function was used in the transmural direction. The final volume mesh of the stomach consisted of 64 nodes and 28 elements.

The torso model was developed in a similar manner, from the 20 labeled points on the torso from the CT images. Four cubic Hermite basis functions were used to fit an ellipsoid around the transverse outline of each torso. The cubic Hermite basis function was also used join the successive ellipsoids together to form the surface mesh of the torso. Triangular elements were used to close the top and bottom of the torso mesh. Each element of the torso mesh was then refined twice in both directions to form the final torso mesh, which contained 624 elements and 306 nodes. Since the BEM was used to solve for the body-surface potentials, a volumetric mesh of the torso with a wall-thickness was not needed.

C. Baseline and Dysrhythmia Models Development

A previously described grid-based FEM scheme was used to simulate gastric slow wave activations across the whole-organ stomach model [20]. A simplified ICC model was used to simulate a single cell activation at each solution point [21],

$$C_m \frac{dV_m}{dt} = I_{Na} + I_{Ca} + I_{BK}$$

where C_m denotes the membrane capacitance of the pacemaker, V_m denotes the membrane potential, I_{Na}, I_{Ca}, and I_{BK}, denote the sodium, calcium and background potassium conductance, respectively. The cell model was coded in the CellML markup standard [22].

The propagation of gastric slow waves was simulated by solving the sequence of pacemaker cell models in continuum, in the form of the bidomain equation,

$$\nabla \cdot (\sigma_i \nabla V_m) = -\nabla \cdot ((\sigma_i + \sigma_e) \nabla \phi_e)$$

$$A_m \left(C_m \frac{dV_m}{dt} + I_{ion} \right) - \nabla (\sigma_i \nabla \phi_e) = \nabla \cdot (\sigma_i \nabla V_m)$$

where σ denotes the conductivity of the tissue, A_m denotes the cell surface-to-volume ratio ($200 \, \text{m}^{-1}$), and I_{ion} is the sum of ion currents through the cell membrane. The equation was solved for 4608 solution points in each whole-organ model.

Based on previously reported experimental data [23], [24], a resting membrane potential gradient of -45 to -75 mV was prescribed to the whole-organ model. The corpus and antrum regions were prescribed an intrinsic frequency gradient of 3 cpm, and the fundus was electrically quiescent [3]. Two sets of whole-organ gastric slow waves simulations were conducted in each subject: 1) normal AW that emerges in the proximal stomach and terminates at the pylorus. The pattern of propagation was based on previously reported baseline human HR mapping data [3]; and 2) colliding of wavefronts, which is a common form of gastric slow wave dysrhythmias observed in patients with motility disorders [6]. In order to keep the collision pattern consistent between subjects, the ectopic activation was assumed to occur from the terminal antrum and propagated in the retrograde direction in the antrum, before colliding with the normal AW activity at the corpus-antrum border.

The net direction of the slow wave activations at each time step was represented by an equivalent fixed position dipole source (J),

$$J = -\sigma (\nabla V_m)$$

The resultant body-surface potentials that arise from underlying gastric slow waves were simulated using a forward simulation. The BEM was employed to simulate potentials over the torso surface [20], by solving the following equation,

$$\nabla \cdot (\sigma_t \nabla \phi) = \nabla \cdot J$$

where σ_t denotes the torso conductivity, which was assumed to homogeneous in the torso cavity, and ϕ denotes body-surface potentials. For ease of comparison between subjects, the body-surface potentials were normalized as follows [25],

$$\bar{\phi} = \frac{\overline{\phi_i} - \phi_{min}}{\phi_{max} - \phi_{min}}$$

The simulations were performed in CMISS on a 48 core high performance computer server (4x Xeon 6136 @ 3 GhZ) with 1.18 TB memory. In each case, the slow waves and resultant body-surface potential (BSP) was simulated over a period of 600 s, with the data output at 1 s intervals.

D. Analysis

The anatomical variations of the stomach were quantified from the fitted geometric models and validated against manual measurements where appropriate. The cavity volume, tissue volume of the active tissues, length of the greater curvature ware calculated from the stomach models. The torso height, circumference, and Euclidean distance between the xiphoid and umbilicus were calculated from the torso models. Specifically, the length of the greater curvature, torso circumference, and distance between the xiphoid and umbilicus were compared against the manual measurements in terms of room-mean-squared (RMS) error and a Student's t-test, where p < 0.05 was deemed as statistically significant.

For each subject, the coverage of a 5×5 array of electrodes on the body-surface was chosen based on the standard placements implemented of previously reported BSGM applications [11], [15]. Simulated slow waves and BSP were further processed using FFT, and the unnormalized amplitudes of the BSP were also measured at the 25 body-surface electrodes. The Pearson correlation coefficient was used to quantify the relationship between the gastric slow wave dipole and the BSP closest to the centroid of the stomach,

$$\rho = \frac{1}{N-1} \sum_{i=1}^{N} \left(\frac{BSP_i - u_{BSP}}{\sigma_{BSP}} \right) \left(\frac{GSD_i - \mu_{GSD}}{\sigma_{GSD}} \right) \tag{1}$$

where body-surface potentials and gastric slow wave dipole are denoted by BSP and GSD, respectively. N is the number of data points over the simulated period, μ and σ are the mean and standard deviation, respectively. The correlation coefficient was also used to show correlation between other features such as age, stomach and torso volume, amplitude of signals.

For each stomach model, the Euclidean distance between the centroid of the stomach and xiphoid, as well as the distance between the centroid of the stomach and the locations of maximum and minimum BSP (ϕ_{max}, ϕ_{min} respectively) were determined. Key BSP features during gastric slow wave activation were quantified based on previously described methods [25]. The difference between ϕ_{max} and ϕ_{min} ($\Delta\phi$) was calculated. The length (L) and the orientation with respect to the X-Z plan (θ) of the vector between the extrema were determined. Finally, average potential attenuation adjacent to the extrema were estimated from the simulated body-surface potentials, by computing the average potential gradients at N points within 70 mm of the extrema.

$$A_{max,min} = \frac{\sum_{i=1}^{N} \frac{\bar{\phi}_i - \overline{\phi_{max,min}}}{d(P_i, P_{max,min})}}{N}$$

where $\bar{\phi}$ is the normalized potential and d is the Euclidean distance between point P_i and the extrema. Each BSP feature was compared between normal and colliding waves during a Student's t-test, where $p < 0.05$ was deemed as statistically significant.

III. RESULTS

A. Variations of Gastric and Torso Anatomy

The stomach anatomy displayed a large degree of biological variability across the 93 subjects studied, as shown in Fig. 3. The average volume of the stomach was 150 ± 85 mL (CI: $132 - 167$ mL) (Fig. 3(a)), which was comparable to previous volume measurements of empty human stomach using polyethylene glycol [26]. There was a gender difference in the volume of the stomach (F vs M, 123 ± 58 mL vs 159 ± 58 mL, $p \approx 0.03$), and age had a low degree of correlation to the volume ($\rho = 0.05$). The average distance from the center of the stomach to xiphoid was 8.6 ± 2.2 cm (CI: $8.1 - 9.0$ cm) (Fig. 3(a)). Overall, 68/93 (74%) stomach models were orientated within $195 \pm 20°$ (CI: $191 - 208°$) relative to the axial plane, with the antrum of the stomach towards the umbilical region.
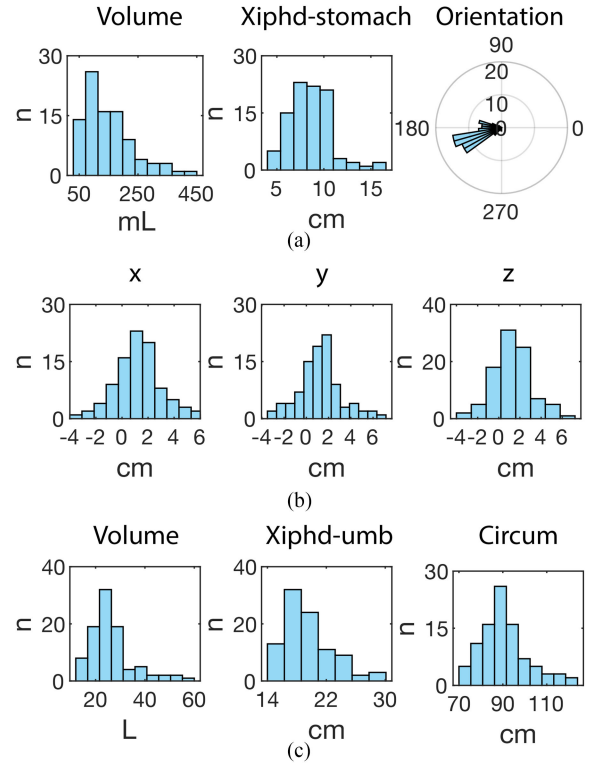

Fig. 3. Distributions of gastric and torso anatomy in all subjects. (a) Gastric volume, distance between xiphoid and stomach, and orientation of the stomach. (b) The x-, y-, and z- positions of the stomach relative to the xiphoid. (c) Torso volume, distance between xiphoid and umbilicus, circumference.

The center of the stomach was generally positioned on the left side of the torso. There was a degree of anatomical variations in the distances of the x-, y- and z- positions of the stomach relative to the xiphoid process, as shown in Fig. 3(b). On average, the stomach was 1.3 ± 1.9 cm (CI: $0.9 - 1.7$ cm) to the left of the xiphoid process in the x-direction, 4.0 ± 1.8 cm (CI: $3.6 - 4.4$ cm) behind the xiphoid process in the y-direction, and 6.7 ± 3.0 cm (CI: $6.1 - 7.3$ cm) below the xiphoid process in the z-direction.

The anatomy of torso was another important factor to consider as it influences the amplitude of BSGM signals. In general, all three metrics measured from the torso models demonstrated some level of left skewness. The mean volume of the torso was 27 ± 9 L (CI: $24.8 - 28.3$ L), without significance difference between females and males ($p \approx 0.51$) and a low correlation with age ($\rho = 0.22$). The mean xiphoid to umbilicus distance was 19.4 ± 3.3 cm (CI: $18.8 - 20.1$ cm), which was comparable to manual measurements (19.7 ± 3.3 cm; RMSE: 0.57 mm; $p > 0.63$). The mean torso circumference was 91 ± 11 cm (CI: $88.4 - 92.9$ cm), which was comparable to manual measurements (92 ± 11 cm; RSME 1.59 mm; $p \approx 0.46$).

B. Antegrade and Retrograde Simulations

A representative example of AW propagation of gastric slow waves is demonstrated in Fig. 4(a). A typical wavefront took approximately 50 s (from 40 to 90 s in Fig. 4(a)) to emerge in the
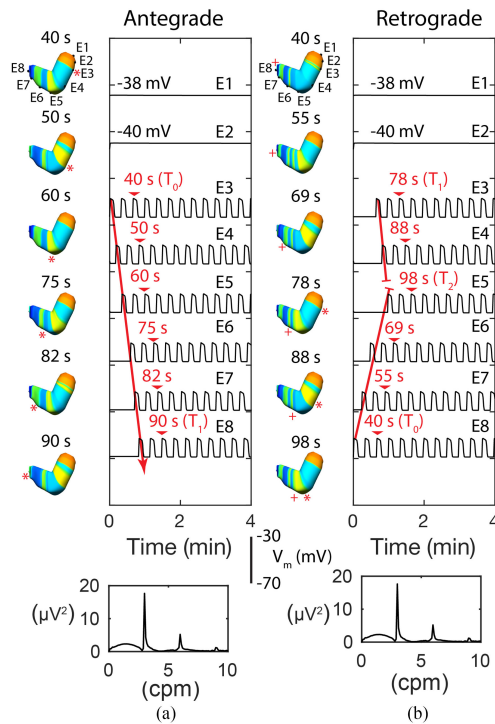
Fig. 4. Whole-organ simulations of gastric slow wave propagations. Eight virtual electrodes (E1-8) were placed along the greater curvature of the stomach. (a) Antegrade simulations of slow waves emerging from the proximal corpus (T_0) and propagating to the pylorus, terminating at T_1. The position of the wavefront is indicated by ∗. (b) Colliding wavefronts between retrograde waves emerging from the distal stomach at T_0 and antegrade waves emerging from the normal pacemaker region at T_1. The collision occurs in the mid corpus of the stomach at T_2. The positions of the antegrade and retrograde wavefronts are indicated by ∗ by +, respectively.

proximal stomach and reach the pylorus. It took approximately 35 s for the wavefront to reach the corpus-antrum border and another 15 s to propagate across the antrum. Due to the frequency of gastric slow waves, there was an "congregation" of wavefronts, e.g., two wavefronts could be observed at 40 s, and up to three simultaneous wavefronts could exist in the stomach at the same time at 82 s, when the repolarization in the distal antrum occurred at the same time as another wave merged in the proximal stomach. The fundus remained depolarized throughout the entire simulations.

The initial 240 s of colliding wavefronts simulation is demonstrated in Fig. 4b. The distal pacemaker initiated a slow wave that propagated in the retrograde direction at 40 s. The velocity of propagation was slower than in the antegrade direction (1.4 mm s^{-1} vs 5.5 mm s^{-1}), as the direction of propagation was against the intrinsic frequency gradient [27]. Approximately 38 s (indicated as 78 s in Fig. 4b) into the retrograde propagation, an AW emerged from the proximal stomach and collided with the retrograde wavefront in the mid corpus.

It is worth nothing that FFT of the resultant dipoles of each activity in Fig. 4 demonstrated near identical dominant frequency (antegrade vs retrograde: 3.0 vs 3.0 cpm), which demonstrates that such analysis could be insufficient in identifying spatial dysrhythmias that occur at the nominal frequency

range [6]. There was also no shift in the power associated with the dominant frequency between the two activities (17.64 μV). When compared across the entire population studied, a similar trend of comparable dominant frequency and powers associated with the dominant frequency (58 ± 33 vs $48 \pm 24 \mu$V; $p \approx 0.13$).

Analysis of the simulated BSGM was done on a segment of simulated data after the resultant dipole had reached steady state, i.e., after at least one cycle of wavefronts had reached the terminal antrum. The average FFT of the BSGM from the 25 electrode potentials was compared to the FFT of gastric dipole and demonstrated identical dominant frequency. The correlation coefficient between the gastric dipole and the body-surface potentials was 0.77 ± 0.29 during AW and 0.68 ± 0.22 during CW.

A number of features could be distinguished between the steady-state solutions of underlying activities and the resultant body-surface potentials, as shown in Fig 5. For the antegrade activity, the clearest indication of the emergence of slow waves in the proximal stomach (T_0 in black) was the minimums of A_{max}, (Fig. 5(d), black dashed line) which was generally located in the proximity of the normal pacemaker region (Fig. 5(a)). On the other hand, the exit of a wavefront in the terminal antrum was indicated by the minimum of A_{min} (Fig. 5(d), black solid line), which was located in the proximity of the terminal antrum. The dominant frequency of $\Delta\Phi$ matched the simulated gastric slow waves (Fig. 5(b)). In the AW case, the termination of waves in the pylorus occurred during the upstroke of $\Delta\Phi$, which was not observed in the CW case. It is also worth noting that due to the speed and frequency of gastric slow waves, each repeating subsequent feature was associated with a preceding wave rather than the present wave. There was also a very minimal change in θ during AW (140-150º) but more pronounced during CW (119-160º), likely due to the opposite directions of the propagating wavefronts. The timing of the collision of waves occurred during the upstroke of θ during CW (Fig. 5(e)).

C. Population Analysis

A number of BSGM characteristics of antegrade and colliding wavefronts demonstrated significant differences when analyzed over the entire cohort, as shown in Fig. 6. Of all the characteristics, only maximum of L and maximum average attenuation of A_{max} did not show a statistical difference between the two types of waves (Fig. 6(b)&(e)). Of the characteristics that demonstrated a difference, the maximum of the average attenuation (A_{max}) and the minimum of $\Delta\Phi$ showed moderate significance ($0.01 < p < 0.05$) (Fig. 6(a)&(d)). There was a strong correlation of 0.58 between $\Delta\Phi$ and the volume of stomach. The remaining characteristics all showed a strong significance between AW and CW. In particular, the difference in θ (AW_{max} vs CW_{max}: $148 \pm 16º$ vs $152 \pm 18º$; $p < 0.001$, AW_{min} vs CW_{min}: $118 \pm 17º$ vs $122 \pm 17º$; $p < 0.004$) suggest that a difference in the orientations of the body-surface potentials could be detected due to the change in the direction of the underlying gastric slow wave activations (Fig. 6(c)).

On average, the maximum and minimum of L was 138 ± 34 mm and 97 ± 31 mm, respectively. This suggests
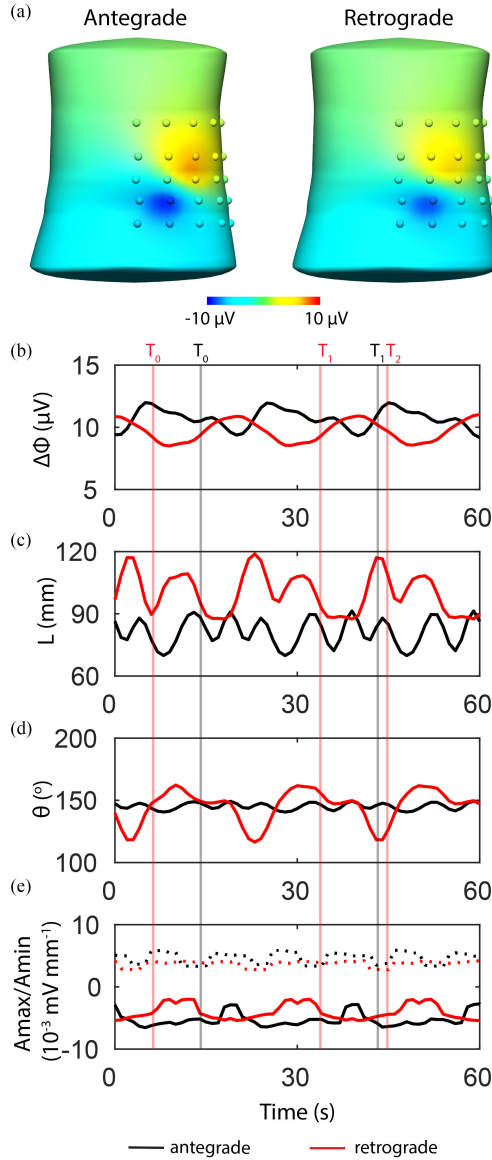
Fig. 5. Torso simulations of antegrade and retrograde gastric slow wave propagations. (a) The simulated data were analyzed over the 25 electrodes on the anterior torso. (b) The difference between extrema. (c) The Euclidean distance between the extrema. (d) The orientation relative to the vertical axis of the torso. (e) The averaged decay near the extrema (solid lines, A_{min}; dashed lines, A_{max}). For the antegrade propagation (black) the activity emerged from the normal pacemaker at T_0 and terminated in the pylorus at T_1. For the retrograde propagation (red) the retrograde activity emerged from the pylorus at T_0 and collided with the antegrade wavefront at T_2. In this case the antegrade wavefront emerged from the normal pacemaker region at T_1. The same time events are also indicated in Fig. 4.
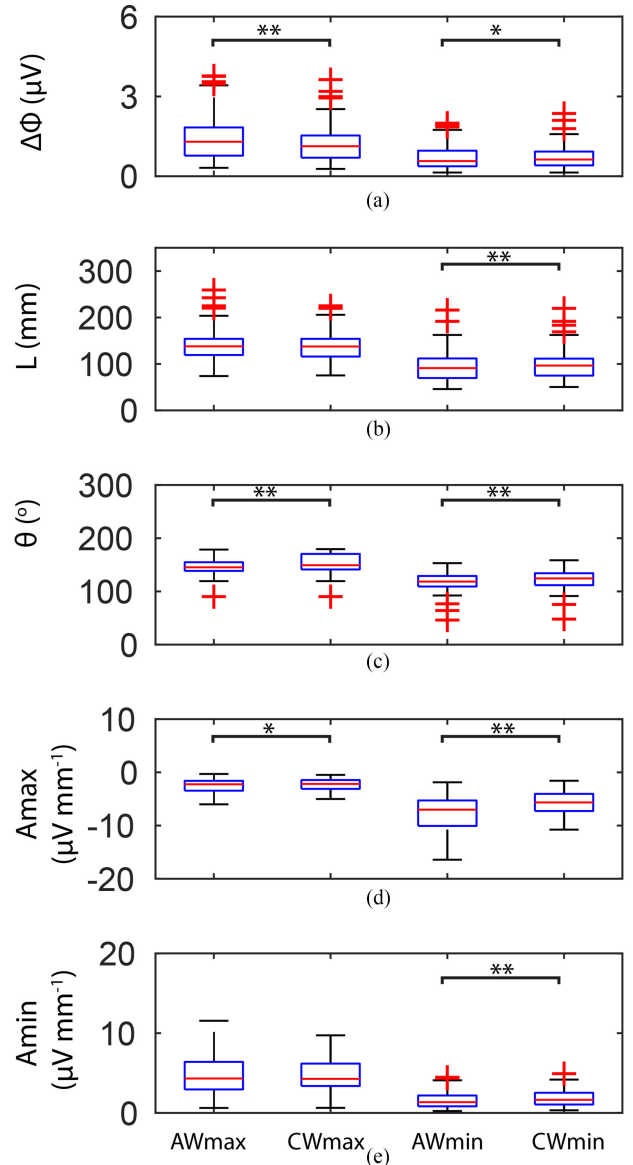

Fig. 6. Population summary of BSGM between antegrade wave (AW) and colliding waves (CW). The maximum and minimum of each characteristic were compared between the two waves. (a) Difference between the extrema of body-surface potentials ($\Delta\Phi$). (b) Distance between the extrema (L). (c) Orientation (θ). (d) Average attenuation around the maximum (A_{max}), (e) Average attenuation around the minima (A_{min}). The black bars represent statistical significance (*p < 0.05; ** p < 0.004).

that an array of electrodes should have at least 140 mm in each dimension to adequately capture the variations between AW and CW, provided the placement of the electrodes are directly over the stomach.

IV. DISCUSSION

This study demonstrated a simulation-based analysis of the population variations of gastric anatomy and its influence on the ability of using multi-channel body-surface gastric mapping (BSGM) to distinguish between antegrade wavefronts (AW) and colliding wavefronts (CW). While significant anatomical variations existed in the cohort of populations studied, features in the BSGM were able to distinguish between CW and AW. In particular, the potential differences between the extrema and orientation of the line connecting the extrema provided potential useful metrics that are sensitive enough to distinguish between AW and CW, which could be captured by an electrode array of at least 140 mm in length coverage. While this study suggested that it would theoretically possible to distinguish between AW and

CW by sampling from a 5×5 array of electrodes, in practice a higher number might be needed to account for the uncertainty in location of the stomach relative to specific anatomical landmarks on the torso.

While a number of previous studies have utilized multiple cutaneous electrodes to determine the general propagation of gastric slow waves [15], [28], a direct relationship between known baseline slow waves could not be elucidated given the inaccessibly of the stomach during the recordings. On the other hand, while invasive serosal HR mapping studies provided detailed activation of the stomach [6], [29], the incision required, sterile field, and the limited duration of recordings in a noisy surgical environment prevented meaningful simultaneous EGG or BSGM to be obtained.

Given the duration of standard gastric emptying tests (240 min), it is likely that future BSGM will require an ambulatory system, which presents a limitation on the number of amplifiers that can be powered on a battery. For a 5×5 grid of electrodes at 20 mm inter-electrode spacing, the coverage is $80 \times 80 \, \text{mm}^2$ [15], so the position of the electrode array would be critical in capturing reliable gastric slow waves in a population. While the anatomical variations of the center of the stomach were comparable to the range of values reported previously using CT images, particularly in the orientation ($195 \pm 20°$ vs $202 \pm 13°$) [15], there are some noticeable differences. First, the present study measured the position from the xiphoid instead of the midpoint of the umbilicus and xiphoid, but the general range of displacements were comparable in all three directions. The one metric that did not produce agreement between the two studies was the volume of the stomach, which was estimated to be 309 ± 176 mL in the previous study and 150 ± 85 mL in the present study. Differences in the volume of oral contrast used and relative time of imaging and oral intake could have contributed to the discrepancy between the two studies. Another potential contributor could be the underestimation of the stomach volume from a single image in the present study.

Another important anatomical factor to consider is the distance of the stomach center to the body-surface, which demonstrated a small variation (8.6 ± 2.2 cm) in the population studied. It is possible that subjects with stomach more towards to the posterior side will need electrodes placed on the flank of the body rather than in the abdominal wall. The orientation of the stomach should be considered as well since the distal region of the human stomach produces the slow waves with the highest amplitude [3], which is more likely to be registered by BSGM.

Conventional EGG has been focusing on a frequency-based approach to classifying gastric slow waves, usually as either bradygastria, tachygastria, or normogastria [9], [30]. As demonstrated in the present study, if the frequency of the distal pacemaker occurs at similar rate to the normal pacemaker, a frequency-based approach is incapable of detecting the spatial dysrhythmias based on the FFT alone (Fig. 4). The no change in power was also expected as the amplitude of the waves did not change between AW and CW, but in practice slow wave dysrhythmias can exhibit change in amplitudes [31]. Therefore,

the power associated with dominant frequency should be compared within the same segment of recording before and after an intervention that has known effect on gastric slow waves [32].

The simulation provided a view of the potential distributions across the entire torso (Fig. 5(a)), which allowed positions of the maximum and minimum potentials to be tracked. The difference between the two extrema provided the theoretical best signal at each instance in time. Based the simulated $\Delta\phi$ (Fig. 5(b)), a 5 s shift in phase of the signals was observed, which would be useful when an intervention such as an electrical stimulus given to alter the conduction of slow waves. Another difference was morphological, i.e., the $\Delta\phi$ associated with AW contained a smaller secondary peak, which was correlated to the emergence of the normal pacemaker. The more pronounced peak in $\Delta\phi$ associated with AW was correlated to the exit of slow waves in the terminal antrum. The occurrence of the two peaks could be explained by the timings when the most significant changes to the dipole had taken place and therefore were reflected in the resultant body-surface potentials. On the other hand, because the waves could "exit" during CW, the peak of the simulated $\Delta\phi$ occurred within the depolarized period following the collision (red T_1 in Fig. 5(b)). Moreover, due to the occurrence of two opposing waves, the simulated $\Delta\theta$ associated with CW was greater than AW (Fig. 5(c)), which may present a useful metric for identifying the general direction if not the variation in the directions of gastric slow waves in BSGM studies.

There are a number of limitations in the present study. The anatomic data was sourced from patients without known stomach complications, which may present different anatomical features due to accumulation of fluid or other gastric content [33]. The current analysis should be extended to gastroparetic patient dataset to explore any potential differences in anatomical features between the control and gastroparetic groups [15]. Despite the statistical difference between the amplitude and orientation metrics (Fig. 6), there was a large amount of overlap between each of the metrics. Therefore, a combination of features from the time series data may be needed in order to distinguish between AW and CW. This could be achieved using a time-series machine learning approach, such as tsfresh [34], to train on a subset of data and cross-validation on simulated and real data [35]. Furthermore, the simulations only represented idealized cases where the AW and CW were stable, without any additional circumferential propagation components that could emanate from a pacemaker [5], [36]. Experimental data have shown a range of dynamic slow wave patterns over time and consistent propagations either occurred in most healthy subjects or achieved via direct electrical stimulation [37], [38], while indirect neuromodulation invoked dynamics changes [27]. It is likely that periods of highly dynamic slow wave dysrhythmias would present a challenge to detection of propagation, so directionality should only be considered during periods with sufficient signal quality. In the present study, the torsos were treated as a homogenous medium, which has been shown to introduce spatial inaccuracies in cardiac simulations [25]. Furthermore, no ventilation or cardiac artifacts were considered in this study,

both of which would present considerable sources of noise to the BSGM signals. Despite these limitations, the investigation was helpful in identifying potential metrics that would be useful as an initial indication of slow wave abnormalities in actual BSGM studies. The torso models could also be refined to include the major organs and skin layers, which would provide a more realistic presentation of the body structure and potentially improve the accuracy of simulations. Given the sensitivity of BSGM to noise, one question that can be addressed by the inhomogeneous models would be the cutoff threshold of BMI for reliable EGG and BSGM recordings.

V. Conclusion

In conclusion, the main outcome of this study was to explore potential differences in simulated BSGM data between antegrade and colliding wavefronts on the stomach. While anatomical variations can impact the signal quality of BSGM data, with consistent placement of recording arrays that have sufficient coverage, combination of metrics could be used to indicate the change in the direction of propagation. However, the significant overlap of any one metric between the two propagations meant definition based a single threshold would be challenging. In future, the proposed metrics and detailed relationship between gastric slow waves and BSGM should be validated in experimental studies with simultaneous recordings from the stomach and body-surface. Such validation will be essential if BSGM will is to succeed in becoming a clinical tool to advance gastric electrophysiology.

References

[1] J. D. Huizinga and W. J. Lammers, "Gut peristalsis is governed by a multitude of cooperating mechanisms," *Amer. J. Physiol. Gastrointest. Liver Physiol.*, vol. 296, no. 1, pp. G1–G8, 2009, doi: 10.1152/ajpgi.90380.2008.

[2] G. O'Grady *et al.*, "Recent progress in gastric arrhythmia: Pathophysiology, clinical significance and future horizons," *Clin. Exp. Pharmacol. Physiol.*, vol. 41, no. 10, pp. 854–862, Oct. 2014, doi: 10.1111/1440-1681.12288.

[3] G. O'Grady *et al.*, "Origin and propagation of human gastric slow-wave activity defined by high-resolution mapping," *Amer. J. Physiol. Gastrointest. Liver Physiol.*, vol. 299, no. 3, pp. G585–G592, 2010, doi: 10.1152/ajpgi.00125.2010.

[4] R. Berry *et al.*, "Functional physiology of the human terminal antrum defined by highresolution electrical mapping and computational modeling," *Amer. J. Physiol. - Gastrointest. Liver Physiol.*, vol. 311, no. 5, pp. G895–G902, 2016, doi: 10.1152/ajpgi.00255.2016.

[5] G. O'Grady *et al.*, "Origin and propagation of human gastric slow-wave activity defined by high-resolution mapping," *Amer. J. Physiol. Liver Physiol.*, vol. 299, no. 3, pp. G585–G592, Sep. 2010, doi: 10.1152/ajpgi.00125.2010.

[6] G. O'Grady *et al.*, "Abnormal initiation and conduction of slow-wave activity in gastroparesis, defined by high-resolution electrical mapping," *Gastroenterology*, vol. 143, no. 3, pp. 583–589, 2012, doi: 10.1053/j.gastro.2012.05.036.

[7] R. Berry *et al.*, "A novel retractable laparoscopic device for mapping gastrointestinal slow wave propagation patterns," *Surg. Endosc. Other Interv. Tech.*, vol. 31, no. 1, pp. 477–486, 2017, doi: 10.1007/s00464-016-4936-4.

[8] T. R. Angeli *et al.*, "High-resolution electrical mapping of porcine gastric slow-wave propagation from the mucosal surface," *Neurogastroenterol. Motil.*, vol. 29, no. 5, 2017, doi: 10.1111/nmo.13010.

[9] N. Wolpert, I. Rebollo, and C. Tallon-Baudry, "Electrogastrography for psychophysiological research: Practical considerations, analysis pipeline, and normative data in a large sample," *Psychophysiology*, vol. 57, no. 9, Sep. 2020, Art. no. e13599, doi: 10.1111/psyp.13599.

[10] H. Murakami *et al.*, "Current status of multichannel electrogastrography and examples of its use," *J. Smooth Muscle Res.*, vol. 49, pp. 78–88, 2013, doi: 10.1540/jsmr.49.78.

[11] A. A. Gharibans *et al.*, "High-Resolution electrogastrogram: A novel, noninvasive method for determining gastric slow-wave direction and speed," *IEEE Trans. Biomed. Eng.*, vol. 64, no. 4, pp. 807–815, Apr. 2017, doi: 10.1109/TBME.2016.2579310.

[12] D. A. Carson *et al.*, "Body surface mapping of the stomach: New directions for clinically evaluating gastric electrical activity," *Neurogastroenterol. Motil.*, vol. 33, Dec. 2020, Art. no. e14048, doi: 10.1111/nmo.14048.

[13] A. S. Agrusa *et al.*, "A deep convolutional neural network approach to classify normal and abnormal gastric slow wave initiation from the high resolution electrogastrogram," *IEEE Trans. Biomed. Eng.*, vol. 67, no. 3, pp. 854–867, Mar. 2020, doi: 10.1109/TBME.2019.2922235.

[14] S. Calder *et al.*, "A simulated anatomically accurate investigation into the effects of biodiversity on electrogastrography (EGG)," *IEEE Trans. Biomed. Eng.*, vol. 67, no. 3, pp. 868–875, Mar. 2020, doi: 10.1109/TBME.2019.2922449.

[15] A. A. Gharibans *et al.*, "Spatial patterns from high-resolution electrogastrography correlate with severity of symptoms in patients with functional dyspepsia and gastroparesis," *Clin. Gastroenterol. Hepatol.*, vol. 17, pp. 2668–2677, Apr. 2019, doi: 10.1016/j.cgh.2019.04.039.

[16] A. Ruenruaysab *et al.*, "Effects of anatomical variations on body surface gastric mapping," in *Proc. IEEE Annu. Int. Conf. Eng. Med. Biol. Soc.*, 2020, pp. 2388–2391.

[17] S. Calder *et al.*, "A theoretical analysis of electrogastrography (EGG) signatures associated with gastric dysrhythmias," *IEEE Trans. Biomed. Eng.*, vol. 64, no. 7, pp. 1592–1601, Jul. 2017, doi: 10.1109/TBME.2016.2614277.

[18] K. Clark *et al.*, "The cancer imaging archive (TCIA): Maintaining and operating a public information repository," *J. Digit. Imag.*, vol. 26, no. 6, pp. 1045–1057, Dec. 2013, doi: 10.1007/s10278-013-9622-7.

[19] P. A. Yushkevich *et al.*, "User-guided 3D active contour segmentation of anatomical structures: Significantly improved efficiency and reliability," *Neuroimage*, vol. 31, no. 3, pp. 1116–1128, Jul. 2006, doi: 10.1016/j.neuroimage.2006.01.015.

[20] P. Du *et al.*, "A multiscale model of the electrophysiological basis of the human electrogastrogram," *Biophys. J.*, vol. 99, no. 9, pp. 2784–2792, 2010, doi: 10.1016/j.bpj.2010.08.067.

[21] P. Du *et al.*, "A simplified biophysical cell model for gastric slow wave entrainment simulation," in *Proc. Conf. Annu. Int. Conf. IEEE Eng. Med. Biol. Soc.*, 2013, vol. 2013, pp. 6547–6550, doi: 10.1109/EMBC.2013.6611055.

[22] C. M. Lloyd *et al.*, "The CellML model repository," *Bioinformatics*, vol. 24, no. 18, pp. 2122–2123, Sep. 2008, doi: 10.1093/bioinformatics/btn390.

[23] J. H. Szurszewski and G. Farrugia, "Carbon monoxide is an endogenous hyperpolarizing factor in the gastrointestinal tract," *Neurogastroenterol. Motil.*, vol. 16, pp. 81–85, 2004, doi: 10.1111/j.1743-3150.2004.00480.x.

[24] M. L. Buist, A. Corrias, and Y. C. Poh, "A model of slow wave propagation and entrainment along the stomach," *Ann. Biomed. Eng.*, vol. 38, no. 9, pp. 3022–3030, 2010, doi: 10.1007/s10439-010-0051-1.

[25] L. R. Bear *et al.*, "Forward problem of electrocardiography: Is it solved?," *Circ. Arrhythm. Electrophysiol.*, vol. 8, no. 3, pp. 677–684, Jun. 2015, doi: 10.1161/CIRCEP.114.001573.

[26] B. Y. Ong, R. J. Palahniuk, and M. Cumming, "Gastric volume and pH in out-patients," *Can. Anaesth. Soc. J.*, vol. 25, no. 1, pp. 36–39, Jan. 1978, doi: 10.1007/BF03006781.

[27] A. Sukasem *et al.*, "The effects of low-and high-frequency non-invasive transcutaneous auricular vagal nerve stimulation (taVNS) on gastric slow waves evaluated using in vivo high-resolution mapping in porcine," *Neurogastroenterol. Motil.*, vol. 32, no. 7, Jul. 2020, Art. no. e13852, doi: 10.1111/nmo.13852.

[28] A. A. Gharibans *et al.*, "Artifact rejection methodology enables continuous, noninvasive measurement of gastric myoelectric activity in ambulatory subjects," *Sci. Rep.*, vol. 8, no. 1, Mar. 2018, Art. no. 5019, doi: 10.1038/s41598-018-23302-9.

[29] T. H.-H. Wang *et al.*, "Slow-wave coupling across a gastroduodenal anastomosis as a mechanism for postsurgical gastric dysfunction: Evidence for a 'gastrointestinal aberrant pathway'," *Amer. J. Physiol. Gastrointest. Liver Physiol.*, vol. 317, no. 2, pp. G141–G146, Aug. 2019, doi: 10.1152/ajpgi.00002.2019.

[30] J. Yin and J. D. Chen, "Electrogastrography: Methodology, validation and applications," *J. Neurogastroenterol. Motil.*, vol. 19, no. 1, pp. 5–17, 2013, doi: 10.5056/jnm.2013.19.1.5.

[31] G. O'Grady *et al.*, "Abnormal initiation and conduction of slow-wave activity in gastroparesis, defined by high-resolution electrical

mapping," *Gastroenterology*, vol. 143, no. 3, pp. 589–598, 2012, doi: 10.1053/j.gastro.2012.05.036.

[32] P. Du *et al.*, "High-resolution mapping of Hyperglycemia-induced gastric slow wave dysrhythmias," *J. Neurogastroenterol. Motil.*, vol. 25, no. 2, pp. 276–285, Apr. 2019, doi: 10.5056/jnm18192.

[33] S. L. Jones and A. T. Blikslager, "Disorders of the gastrointestinal system," in *Equine Internal Medicine*. Amsterdam, Netherlands: Elsevier, 2004, pp. 769–949.

[34] M. Christ *et al.*, "Time series feature extraction on basis of scalable hypothesis tests (tsfresh – a python package)," *Neurocomputing*, vol. 307, pp. 72–77, Sep. 2018, doi: 10.1016/j.neucom.2018.03.067.

[35] D. E. Dempsey *et al.*, "Automatic precursor recognition and real-time forecasting of sudden explosive volcanic eruptions at whakaari, New Zealand," *Nature Commun.*, vol. 11, no. 1, Dec. 2020, Art. no. 3562, doi: 10.1038/s41467-020-17375-2.

[36] W. J. Lammers *et al.*, "Peripheral pacemakers and patterns of slow wave propagation in the canine small intestine in vivo," *Can. J. Physiol. Pharmacol.*, vol. 83, no. 11, pp. 1031–1043, 2005, doi: 10.1139/y05-084.

[37] G. O'Grady *et al.*, "High-resolution entrainment mapping of gastric pacing: A new analytical tool," *Amer. J. Physiol. Gastrointest. Liver Physiol.*, vol. 298, no. 2, pp. G314–G321, 2010, doi: 10.1152/ajpgi.00389.2009.

[38] P. Du *et al.*, "A tissue framework for simulating the effects of gastric eelectrical stimulation and in vivo validation," *IEEE Trans. Biomed. Eng.*, vol. 56, no. 12, pp. 2755–2761, Dec. 2009, doi: 10.1109/TBME.2009.2027690.